Journal of Aerosol Science 169 (2023) 106134

Contents lists available at ScienceDirect

Journal of Aerosol Science

journal homepage: www.elsevier.com/locate/jaerosci

Clustering and collision of Brownian particles in homogeneous and isotropic turbulence

Tianyi Wu [a,b], Sheng Chen [a,*], Pinzhuo Chen [a], Shuiqing Li [b]

[a] State Key Laboratory of Coal Combustion, School of Energy and Power Engineering, Huazhong University of Science and Technology, Wuhan, 430074, China
[b] Key Laboratory for Thermal Science and Power Engineering of Ministry of Education, Department of Energy and Power Engineering, Tsinghua University, Beijing, 100084, PR China

ARTICLE INFO

Keywords:
Nanoparticles
Particle agglomeration
Collision kernel
Flame synthesis
Homogeneous isotropic turbulence
Population balance modelling

ABSTRACT

The collision rate between primary nanoparticles in the turbulent flow is of significance for accurately predicting the growth rate of agglomerates during the flame synthesis process. In this work, the clustering and the collision of Brownian particles in the free-molecular regime in homogeneous isotropic turbulence are investigated using the direct numerical simulation and the Langevin dynamics. It is found that the Brownian motion can distribute the particles more uniformly, leading to the formation of a plateau on the curve of the radial distribution function (RDF). This anti-clustering effect is significant only at a small separation distance of particle pairs and cannot be observed when the separation is larger than a critical value. The radial relative velocity (RRV) is significantly enhanced, especially at the small separation distance, when the Brownian motion is taken into account. A velocity superposition analysis shows that the statistics of RRV of Brownian particles can be obtained by adding a random variable onto the RRV of non-Brownian particles with the same Stokes number. The increased radial relative velocity counteracts the anti-clustering effect of the Brownian motion and leads to the increase of the geometric collision kernel. Finally, the collision kernel of Brownian particles is formulated as a function of asymptotic values of RDF and RRV at a vanishing separation. The proposed collision kernel enables us to estimate the collision rate between nanoparticles that are much smaller than the Kolmogorov length scale.

1. Introduction

Collision and agglomeration of nanoparticles in turbulence are ubiquitous in many natural and industrial processes, including the flocculation during water treatment (Renault et al., 2009; Verma et al., 2012), atmospheric processes (Ziemann & Atkinson, 2012), the aerosol formation (Morán et al., 2021; Wang & Chung, 2019), the material synthesis in flames (Bringley et al., 2022; Li et al., 2016; Rai et al., 2018), and the particulate matter capture (Chen et al., 2016; Jaworek et al., 2018; Li & Marshall, 2007). In real industry applications, tracking the dynamics of every individual particle is far beyond the computational capability. Therefore, the population balance equation (PBE), which statistically describes the evolution of the size distribution of agglomerates at the macroscopic continuum level, is one of the few theoretical tools that can be applied to large-scale systems (Boje & Kraft, 2022; Chen et al., 2021; Hou

* Corresponding author.
E-mail address: sheng_chen@hust.edu.cn (S. Chen).

https://doi.org/10.1016/j.jaerosci.2022.106134
Received 29 May 2022; Received in revised form 28 December 2022; Accepted 29 December 2022
Available online 30 December 2022
0021-8502/

et al., 2020; Huang et al., 2017; Ramkrishna & Singh, 2014; Sharma et al., 2019; Wang et al., 2019; Zhang et al., 2020). The most important component in PBE is the collision kernel that characterizes how fast agglomerates of size *i* collide with agglomerates of size *j*. For nanoparticles immersed in a turbulent flow, both the random Brownian motion and the coherent vortex structures affect the clustering and collision between particles (Polovnikov et al., 2016; Cifuentes et al., 2020; Hitimana et al., 2021). However, a collision kernel that can simultaneously reflect the influences of the turbulent transport and the random Brownian motion is still lacking. The current work, therefore, focuses on the collision rate of nanoparticles in the free-molecular regime in turbulence.

There have been extensive investigations on the collision kernel of non-Brownian inertial particles in turbulence. The collision kernel is usually expressed as a function of the mean radial inward velocity and the radial distribution function (RDF) of particle pairs at the distance of the contact. Particles with negligible inertia are uniformly distributed in the flow field and the mean radial inward velocity can be determined from the velocity gradient of turbulence flows (Saffman & Turner, 1956). The influence of particle inertia on the collision kernel is then discussed, identifying the effect of the preferential concentration (Balachandar & Eaton, 2010; Lian et al., 2019; Saw et al., 2008; Squires & Eaton, 1991; Tagawa et al., 2012; Yuan et al., 2018), which results in inhomogeneous particle distribution (particles clustering) in turbulence, and the sling or caustic effect (Falkovich et al., 2002; Pumir & Wilkinson, 2016; Wilkinson et al., 2006), which makes inertial particles to collide with large velocity differences. The clustering of particles can be statistically characterized by RDF, which depends on both the separation distance and the particle inertia. For a given separation, RDF first increases and then decreases with the particle Stokes number (St). The peak of the RDF shifts to a higher St value with the increasing separation distance. For a fixed value of St, RDF approaches the unity at the large separation limit (Gustavsson & Mehlig, 2016; Ray & Collins, 2011; Reade & Collins, 2000). Complicated interparticle interactions, including the elastic repulsion (Bec et al., 2013; Voßkuhle et al., 2013), the electrostatic interactions (Lu et al., 2010; Lu & Shaw, 2015; Ruan et al., 2021), and the van der Waals adhesion (Kellogg et al., 2017; Dizaji & Marshall, 2016; 2018; Chen et al., 2019; Zhao et al., 2020; Mortimer, Njobuenwu, & Fairweather, 2020; Chen & Li, 2020), have been considered in several recent studies and give rise to non-trivial collision phenomena.

The collision rate of Brownian particles in turbulence, in contrast, is far from clear. Previous studies mainly focus on the collision rate caused solely by the random Brownian motion with little consideration for the turbulent effect. For Brownian particles in the continuum regime (i.e. with a Knudsen number $\mathrm{Kn} \ll 1$), the particle moves in a random, meandering path, and the collision can be described as a Brownian diffusion process that is affected by the hydrodynamic drag (Fuchs, 1964). For nanoparticles in the free-molecular regime ($\mathrm{Kn} \gg 1$), the collision kernel is similar to that of a gas molecule (Glassman & Yetter, 2008). The drag force on particles in the free-molecular regime is much less than that predicted from the Stokes law (Buckley & Loyalka, 1989), particles' trajectories, therefore, can deviate from the streamlines despite the small inertia of particles. The Brownian collision kernels are then modified to account for the effect of non-spherical particle shapes or irregular agglomerate structures (Chen et al., 2019; Endres et al., 2021; Gspann et al., 2017; Qian et al., 2022), the van der Waals force (Jiang et al., 2020; Qian et al., 2022), the electrostatic and magnetic interactions (Li & Gopalakrishnan, 2021; Tsouris & Scott, 1995; Zhang et al., 2011), and the high particle concentration (Heine & Pratsinis, 2007). The coagulation rate, which is highly relevant to the collision rate of aerosols, has been investigated (Chun & Koch, 2005; Garrick, 2011). However, to the best of our knowledge, none of the modifications on the collision kernel above has included the turbulent effect. The current work discusses the collision of nanoparticles in homogeneous isotropic turbulence in the context of flame synthesis, in which the high temperature and the low pressure make the gas mean free path length larger than the particle size (Janzen & Roth, 2001; Lindackers et al., 1997; Qian et al., 2022; Suh et al., 2001). Therefore, the simulation results here are relevant for nanoparticles in the free molecular regime. The particle volume fraction is about the order of 10^{-8} in the flame synthesis process (Camenzind et al., 2008; Zhang et al., 2013).

Recently, the collision of fractal agglomerates in the free-molecular regime is simulated using Langevin dynamics, in which the detailed translational and rotational movements of particles subject to Brownian motion are tracked. Based on the results from the Langevin simulation, a linear relationship between the collision radii and the radius of gyration is proposed, in which the slope and intercept account for the dependence on the shape anisotropy and the fractal dimension (Qian et al., 2022). The Langevin dynamics method, coupled with the direct numerical simulation (DNS), should be able to simulate the clustering and collision of Brownian particles in turbulence (Choi et al., 2015; Friedlander, 2000; Inci et al., 2017; Mofakham & Ahmadi, 2019). However, the related research is deficient leaving many questions to be answered. For example, the Brownian motion intuitively tends to distribute the particles uniformly and inhibit the clustering. However, it is not clear to what extent the anti-clustering effect due to the Brownian motion can counteract the preferential concentration phenomenon for particles in turbulence. Moreover, the anti-clustering effect and the fluctuating Brownian motion have negative and positive impacts on the collision rate, respectively. A quantitative model of the collision rate for Brownian particles considering these two competing effects is still lacking.

In this study, we try to answer the questions above by simulating the motion of Brownian particles in homogenous isotropic turbulence. The flow field is calculated by the direct numerical simulation and the Brownian motion of nanoparticles is simulated using the Langevin equation. We focus on the collision of nanoparticles in the free-molecular regime, where the friction coefficient of the fluid resistance on particles is derived from the gas kinetic theory. The radial distribution function (RDF) and the radial relative velocity (RRV) are calculated for particles with different levels of inertia and Brownian motion intensity. We demonstrate that the Brownian motion has a significant impact on RDF and RRV when the particle separation is below a certain value. A velocity superposition analysis is then proposed to statistically predict the RRV of Brownian particles. At last, the collision kernel for Brownian particles is formulated as a function of the particle Stokes number, the Peclet number, and the collision radius.

2. Numerical methods

2.1. Governing equations and numerical method

The homogeneous and isotropic turbulent (HIT) flow is simulated by the open-source code HIT3d (Chumakov, 2006). The Navier-Stokes equations are solved using the pseudospectral method with second-order Adams-Bashforth time stepping

$$\nabla \cdot \boldsymbol{u}_f = 0, \tag{1a}$$

$$\frac{\partial \boldsymbol{u}_f}{\partial t} + \boldsymbol{u}_f \cdot \nabla \boldsymbol{u}_f = -\frac{1}{\rho_f}\nabla p + \nu \nabla^2 \boldsymbol{u}_f + \boldsymbol{f}_{\boldsymbol{F}}. \tag{1b}$$

Here, $\boldsymbol{u}_f$ is the fluid velocity vector, ρ_f is the fluid density, p is the pressure, and ν is the fluid kinematic viscosity. A statistically stationary state is achieved by imposing the deterministic forces $\boldsymbol{f}_{\boldsymbol{F}}$ to the two lowest wavenumbers in the Fourier space. The numerical simulation domain is a triply periodic cube with a size of 2π in dimensionless unit and is discretized with 128 cells in each direction. The Reynolds number based on the Taylor microscale is $\mathrm{Re}_\lambda = 80$. The maximum wavenumber κ_{max} used in the pseudospectral method and the Kolmogorov length scale η satisfy $\kappa_{max}\eta = 1.55 > 1.5$, indicating that the grid spacing is small enough to resolve the motions at the Kolmogorov scale (Pope, 2000).

Monodisperse nanoparticles are then randomly seeded in the HIT and are tracked through the one-way point-particle Lagrange method. The Brownian motion of particles is modeled by the Langevin equation, in which a random Brownian force is applied to particles. The governing equation for particle motion thus is given by (Friedlander, 2000; Maxey & Riley, 1983):

$$\frac{\mathrm{d}\boldsymbol{x}_{p,i}}{\mathrm{d}t} = \boldsymbol{v}_{p,i}, \tag{2a}$$

$$m_p \frac{\mathrm{d}\boldsymbol{v}_{p,i}}{\mathrm{d}t} = -f\left(\boldsymbol{v}_{p,i} - \boldsymbol{u}_{f,i}\right) + \boldsymbol{F}_{B,i}. \tag{2b}$$

Here, $\boldsymbol{x}_{p,i}$, $\boldsymbol{v}_{p,i}$, and m_p denote the position, velocity, and mass of particle i, $\boldsymbol{u}_{f,i}$ is the fluid velocity at the position of particle i, and $\boldsymbol{F}_{B,i}$ denotes the Brownian force. The current work focuses on particles in the free-molecular regime, therefore, the friction coefficient f is given by (Friedlander, 2000; Epstein, 1924):

Table 1
Physical and dimensionless value of parameters used in the simulations.

Parameters	Physical values	Dimensionless values
Typical scales		
Typical length, L_0	1×10^{-2} m	1
Typical velocity, U_0	40 m/s	1
Typical time, T_0	2.5×10^{-4} s	1
Typical mass, M_0	1.33×10^{-8} kg	1
Fluid properties		
Fluid density, ρ_f	1.33×10^{-2} kg/m^3	1
Fluid kinematic viscosity, ν	3×10^{-3} m^2/s	7.5×10^{-3}
Fluid temperature, T	900 K	–
Fluid pressure, p	3500 Pa	1.64×10^2
Gas mean free path length, λ	5900×10^{-9} m	5.9×10^{-4}
Grid resolution, N^3	128^3	–
Taylor-scale Reynolds number, Re_λ	–	80
Kolmogorov length scale, η	2.59×10^{-4} m	2.59×10^{-2}
Kolmogorov time scale, τ_η	2.23×10^{-5} s	8.92×10^{-2}
Kolmogorov velocity scale, u_η	11.6 m/s	0.29
Mean energy dissipation, ε	6.03×10^6 m^2/s^3	0.94
Root mean square velocity, u_{rms}	53.2 m/s	1.33
Grid spacing, Δx	4.91×10^{-4} m	4.91×10^{-2}
Fluid time step, Δt_f	2.5×10^{-8} s	1×10^{-4}
Particle properties		
Particle density, ρ_p	$1.15 \times 10^3 - 17.25 \times 10^3$kg/m^3	$8.65 \times 10^4 - 1.3 \times 10^6$
Particle diameter, d_p	$4.25 \times 10^{-9} - 12.7 \times 10^{-9}$m	$4.25 \times 10^{-7} - 1.27 \times 10^{-6}$
Particle number, N_p	$10^5 - 5 \times 10^5$	–
Particle volume fraction, φ	$1.62 \times 10^{-17} - 2.16 \times 10^{-15}$	–
Particle time step size, Δt_p	2.5×10^{-9} s	1×10^{-5}
Kolmogorov-scale Stokes number, St_k	–	$0.022 - 0.112$
Kolmogorov-scale Peclet number, Pe_k	–	$3.0 - \infty$

$$f = \frac{2}{3} d_p^2 \rho_f \sqrt{\frac{2\pi k_B T}{m_f}} \left(1 + \frac{\pi\alpha}{8}\right), \tag{3}$$

where d_p is the particle diameter, m_f is the mass of the gas molecules, the momentum transfer coefficient α is set as 0.9, $k_B = 1.38 \times 10^{-23}$ J/K is the Boltzmann constant, and T is the absolute temperature (K) of the fluid. The three components of the Brownian force, $\boldsymbol{F}_B$, in x, y, and z directions are given as (Langevin, 1908; Li & Ahmadi, 1992):

$$F_{B,x/y/z} = G\sqrt{\frac{2k_B T f}{\Delta t_p}}, \tag{4}$$

where G is an independent Gaussian random number with zero mean value and the unit variance and Δt_p is the particle simulation time step. The particle simulation time step Δt_p is set as $\Delta t_p = \left(\frac{d_p^2 m_p^2}{6 f k_B T q}\right)^{\frac{1}{3}}$, and the coefficient $q = 0.263$ (Suresh & Gopalakrishnan, 2021).

2.2. Simulation conditions

Monodisperse particles are randomly seeded into the domain after the turbulence reaching the statistical equilibrium state. The typical velocity is given by $U_0 = 40$ m/s, and the typical length is set as $L_0 = 1 \times 10^{-2}$ m. The typical time thus is $T_0 = L_0/U_0 = 2.5 \times 10^{-4}$ s and the typical mass is $M_0 = L_0^3 \rho_f = 1.33 \times 10^{-8}$ kg, with the fluid density being $\rho_f = 1.33 \times 10^{-2}$ kg/m^3. The velocity, length, and time in Eq. (2) are then normalized by U_0, L_0, and T_0, respectively. The temperature of the surrounding gas is assumed to be $T =$ 900 K and the pressure is $p = 3500$Pa. At this temperature, the fluid kinematic viscosity is $\nu = 3 \times 10^{-3}$ m^2/s. Other relevant parameters, including the particle density and the particle diameter, are summarized in Table 1 in both dimensional and dimensionless forms. The fluid-to-particle density ratio ($\chi = \rho_f/\rho_p$) satisfies $\chi \ll 1$ and the particle volume fraction satisfies $\varphi < 10^{-10}$, indicating that the added mass effect and the turbulent modulation due to particles are negligible in this work.

Since a small particle time step is adopted in our simulation to detect the particle collisions, a huge particle number will lead to an unacceptable computational cost. We use a particle volume fraction that is smaller than the value in a real flame synthesis process. The statistics of the radial distribution function (RDF), the radial relative velocity (RRV), and the geometric collision kernels in the current work should be independent of particle concentration once the sample is large enough. To verify this point, testing simulations are performed using different particle numbers (0.5×10^5, 1×10^5, and 2.5×10^5) and the results of RDF, RRV, and the geometric collision kernel are not affected by the particle number.

The dimensionless form of Eq. (2b) is expressed as:

$$\frac{d\widehat{\boldsymbol{v}}_p}{d\widehat{t}} = -\frac{\widehat{\boldsymbol{v}}_p - \widehat{\boldsymbol{u}}_f}{\mathrm{St}} + \frac{1}{\sqrt{\Delta\widehat{t}_p}} \frac{1}{\mathrm{St}\sqrt{\mathrm{Pe}}} \left(G_1 \boldsymbol{e}_x, G_2 \boldsymbol{e}_y, G_3 \boldsymbol{e}_z\right). \tag{5}$$

Here, $\widehat{v}_p = v_p/U_0$ and $\widehat{u}_f = u_f/U_0$ are the dimensionless velocities of particles and fluid, respectively, $\widehat{t} = t/T_0$ and $\Delta\widehat{t}_p = \Delta t_p/T_0$ are the dimensionless time and dimensionless particle time step, respectively. The macroscopic Stokes number is calculated as $\mathrm{St} = \tau_p/T_0$, where $\tau_p = m_p/f$ is the response time of particles. The Kolmogorov scale Stokes number, representing the inertia of particles, is defined as $\mathrm{St}_k = \tau_p/\tau_\eta$, where $\tau_\eta = \eta/u_\eta$ is the Kolmogorov time scale, η and u_η are the Kolmogorov length and velocity, respectively. The Peclet number $\mathrm{Pe} = U_0 L_0/(2D)$ represents the relative intensity of the advective transport and the Brownian motion with $D = k_B T/f$ being the coefficient of diffusion. The Kolmogorov scale Peclet number is defined as $\mathrm{Pe}_k = u_\eta \eta/(2D)$. Here, $\boldsymbol{e}_x$, $\boldsymbol{e}_y$, and $\boldsymbol{e}_z$ are unit vectors in the x, y, and z directions, respectively, and G_1, G_2, and G_3 are zero-mean, unit variance independent Gaussian random numbers. Hereinafter, all variables are in their dimensionless forms but the same notations are adopted for simplicity.

The current work focuses on the effect of the random Brownian motion on the clustering of particles in HIT. Therefore, the value of the Kolmogorov scale Peclet number is varied within the range $\mathrm{Pe}_k = 3.0 - \infty$, where $\mathrm{Pe}_k \to \infty$ represents no Brownian motion for particles. The value of the Stokes number St_k is varied within the range $\mathrm{St}_k = 0.022 - 0.112$ to reflect the influence of particle inertia.

2.3. Characterization of particle clustering and collision

The clustering and collision of Brownian particles in the homogeneous and isotropic turbulence are characterized in terms of the collision kernel Γ, the radial distribution function (RDF) $g(r)$, and the radial relative velocity (RRV) $w_r(r)$. Here, r is the separation distance between two particles. The radial distribution function is defined as the ratio of the number of particle pairs per unit volume found at a given separation to the expected number if the particles were uniformly distributed (McQuarrie, 1976). RDF can be computed from a field of N_p particles according to

$$g(r) = \frac{N(r)/\Delta V}{N_t/V}, \tag{6}$$

where $N(r)$ is the average number of particles found in an elemental shell volume $\Delta V = 4\pi r^2 \Delta r$ at a separation distance r from a reference particle, V is the volume of the entire simulation domain, and $N_t = N_p(N_p - 1)/2$ is the total number of particle pairs in the system.

The radial relative velocity between particle i and particle j with a separation distance r is calculated as

$$w_r(\boldsymbol{r}) = \left(\boldsymbol{v}_{p,j}(\boldsymbol{x}+\boldsymbol{r}) - \boldsymbol{v}_{p,i}(\boldsymbol{x})\right)\cdot\widehat{\boldsymbol{r}}, \tag{7}$$

where $\boldsymbol{v}_{p,i}(\boldsymbol{x})$ and $\boldsymbol{v}_{p,j}(\boldsymbol{x}+\boldsymbol{r})$ are the velocities of two particles located at $\boldsymbol{x}$ and $\boldsymbol{x}+\boldsymbol{r}$, respectively, and $\widehat{\boldsymbol{r}} = \boldsymbol{r}/|\boldsymbol{r}|$ is a unit vector pointing along their line-of-centers.

The collision kernel based on the direct counting of collision events is given by

$$\Gamma_{ij} = \frac{\dot{\mathcal{N}}_{ij}}{n_i n_j}, \tag{8}$$

where $\dot{\mathcal{N}}_{ij}$ is the collision rate per unit volume and n_i is the average number concentration of size group i. According to the model proposed by Sundaram and Collins (1997), the normalized collision number Z over a time period τ is

$$Z(\tau) = \int\int \Phi(\boldsymbol{r},\boldsymbol{w};\tau)P(\boldsymbol{w}|\boldsymbol{r})g(\boldsymbol{r})\mathrm{d}\boldsymbol{r}\mathrm{d}\boldsymbol{w}, \tag{9}$$

where $\boldsymbol{w}$ is the relative velocity, $\boldsymbol{r}$ is the separation vector between particles, $P(\boldsymbol{w}|\boldsymbol{r})$ is the conditional probability density function (PDF) of the relative velocity at a given separation vector, $\Phi(\boldsymbol{r},\boldsymbol{w};\tau) = H(\boldsymbol{r} - \widetilde{\boldsymbol{r}}(\tau^*))$ is the collision operator with Heaviside function H and $\widetilde{\boldsymbol{r}}(\tau^*)$ represents the minimum separation at time τ^*. The collision kernel is then estimated from the limit $\Gamma = \lim_{\tau\to 0}\frac{Z(\tau)}{\tau} = \frac{\mathrm{d}Z(0)}{\mathrm{d}\tau}$. For homogeneous and isotropic system, the collision kernel for monodisperse particles at separation distance r can be estimated from $g(r)$ and $w_r(r)$ as

$$\Gamma(r) = 4\pi r^2 g(r)\int_{-\infty}^{0} -w_r(r)P(w_r|r)\mathrm{d}w_r, \tag{10}$$

where $g(r)$ denotes the value of the radial distribution function (RDF) at separation distance r, w_r denotes the radial relative velocity, and $P(w_r|r)$ is the conditional probability density function (PDF) of the radial relative velocity at a given separation distance. The collision kernel is usually normalized by the collision kernel of the zero-inertia particles in HIT expressed as (Saffman & Turner, 1956):

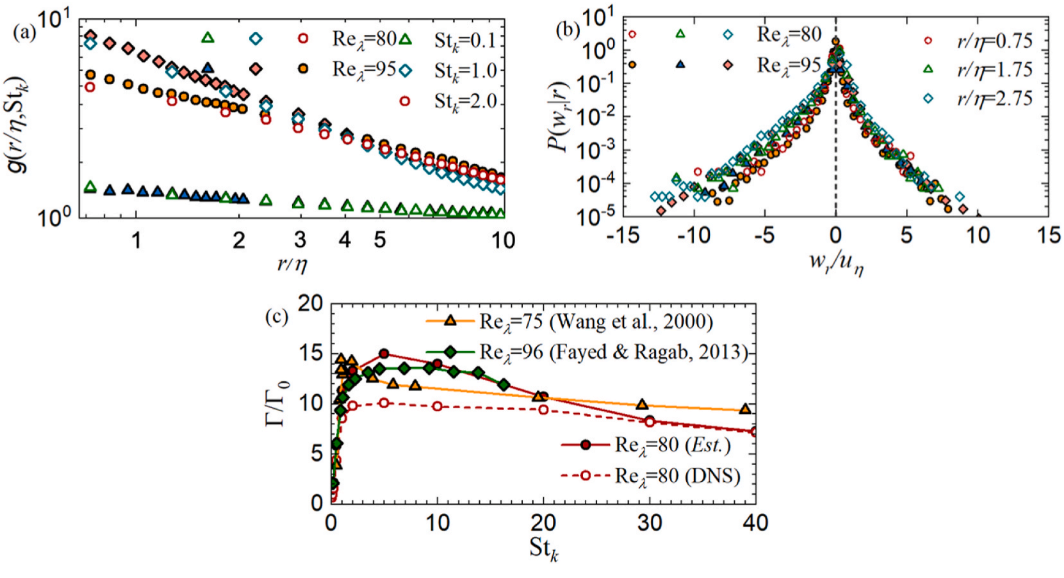

Fig. 1. (a) Variation of the radial distribution function $g(r/\eta, \mathrm{St}_k)$ with the scaled separation distance r/η for $\mathrm{St}_k = 0.1$ (triangles), 1.0 (circles), and 2.0 (diamonds). (b) Probability density function of the radial relative velocity $w_r(r)$ (scaled by the Kolmogorov velocity u_η) at different separation distances: $r/\eta = 0.75$ (circles), 1.75 (triangles), and 2.75 (diamonds) at $\mathrm{St}_k = 1.0$. The open symbols in these two panels are results from our simulation at $\mathrm{Re}_\lambda = 80$ and the solid points are simulation results from (Ray & Collins, 2011) at $\mathrm{Re}_\lambda = 95$. (c) Collison kernel Γ, scaled by the collision kernel of zero-inertia particles Γ_0, as a function of the Stokes number St_k from our simulation based on the direct counting (open circles) or estimated from the radial distribution function and the radial relative velocity (solid circles) at $\mathrm{Re}_\lambda = 80$. Results from Wang et al. (2000) (triangles) at $\mathrm{Re}_\lambda = 75$ and Fayed and Ragab (2013) (diamonds) at $\mathrm{Re}_\lambda = 96$ are also plotted for comparison.

$$\Gamma_0(r) = \sqrt{\frac{8\pi}{15}} r^3 \frac{u_\eta}{\eta}. \tag{11}$$

2.4. Model validations

To validate the simulation method, we first turn off the Brownian force (i.e., $\boldsymbol{F}_B = \boldsymbol{0}$) and compare the simulation results with data in literature for non-Brownian inertia particles. The parameters in this validation case are not the same as the particle flame synthesis conditions in the results section. Since there is no available data for particles in the free-molecular regime in homogeneous isotropic turbulence. The Stokes number St_k is varied from 0.01 to 40 by varying the particle density. The particle diameter is set as 0.75η. Other setups are the same as Brownian particle simulations. The radial distribution function $g(r)$ is plotted as a function of the separation distances (scale by the Kolmogorov length scale η) in Fig. 1(a) for $\mathrm{St}_k = 0.1$, 1.0, and 2.0 and $\mathrm{Re}_\lambda = 80$. The value of $g(r)$ at a given r/η increases with St_k for low St_k, but decreases with St_k for high St_k. The results are in accord with previous findings that clustering is most remarkable for particles with $\mathrm{St}_k = \mathrm{O}(1)$. The DNS simulation results from Ray and Collins (2011) are also plotted in Fig. 1(a) for comparison. A good agreement can be observed between the two data sets. The probability density function of the radial relative velocity w_r, normalized by Kolmogorov velocity scale u_η, at different separation distances $r/\eta = 0.75$, 1.75, and 2.75 are shown in Fig. 1 (b). Again, there is a good agreement between results from the current simulation and those in (Ray & Collins, 2011). In Fig. 1(c), we compare the collision kernels, which are calculated according to the direct counting (Eq. (8)) from DNS and to the model in Eq. (10), respectively, with those in literature. Overall, the simulation results from the current DNS simulation agree well with those from literature, indicating that the simulation method can correctly capture the effect of particle inertia on clustering.

In the second part of the validation, we simulate the three-dimensional Brownian motion of 5000 particles in a stationary flow (i.e. $\boldsymbol{u}_f = \boldsymbol{0}$) using the Langevin equation (Eq. (2)) and compare the results with the solution of the diffusion equation, which is written as

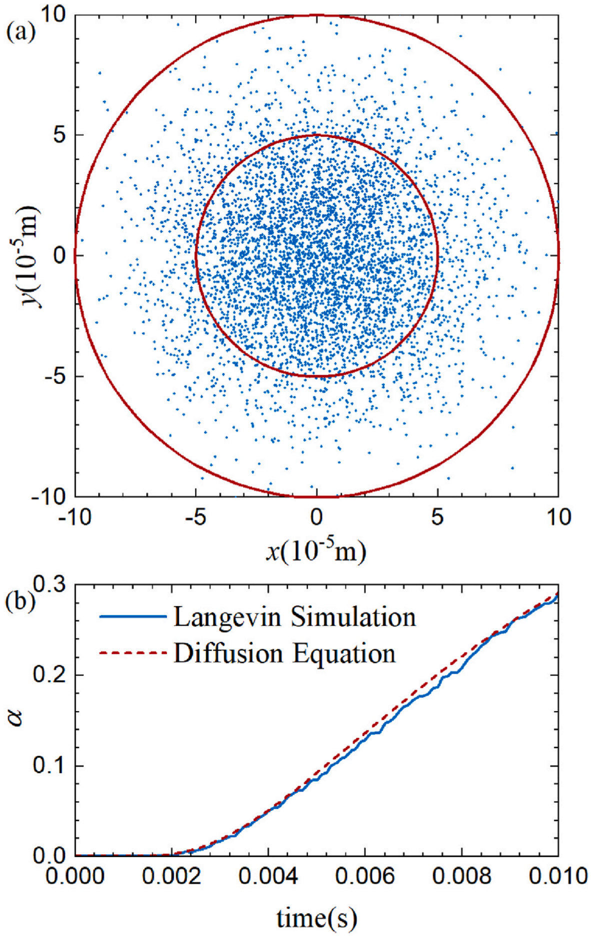

Fig. 2. (a) Spatial distribution of particles at $t = 0.01$ s. The inner domain is the region enclosed by the smaller circle and the outer domain is the region between the two circles. (b) Evolution of the transmission probability obtained by the Langevin simulation (solid line) and the solution of the diffusion equation (dashed line). The definition of the transmission probability is given in Eq. (13) and Eq. (14).

$$\frac{\partial c}{\partial t} + \nabla \cdot (-D\nabla c) = 0. \tag{12}$$

Here, c denotes the particle concentration and D is the coefficient of diffusion, expressed as $D = k_B T/f$. The particles are initially placed at the origin, $c(t=0) = \delta(0,0,0)$. The particle diameter d_p is 1×10^{-8}m, the temperature is $T = 300\ K$, and the corresponding coefficient of diffusion is $D = 5.2 \times 10^{-8}\ \mathrm{m}^2/\mathrm{s}$ in this validation case.

The spatial distribution of particles at $t = 0.01$ s is shown in Fig. 2 (a). As we can see, the Brownian force leads to the spreading of particles from regions of higher particle concentration to lower concentration. The transmission probability is calculated in both the Langevin simulation and the diffusion equation. The transmission probability (termed as α_L and α_D for Langevin simulation and solution of the diffusion equation, respectively) is defined as the fraction of particles that move from the inner domain (enclosed by the inner circle in Fig. 2 (a)) to the outer one (the region between two circles). For particles modeled by the Langevin equation, α_L is calculated by dividing the number of particles in the outer domain N_o by the total particle number N_p, while in the solution of the diffusion equation, α_D is the ratio of the integral of the concentration over the outer domain to the integral over both the inner and outer regions. The expressions are as follows

$$\alpha_L = \frac{N_\mathrm{O}}{N_p}, \tag{13}$$

$$\alpha_D = \frac{\int_{\mathrm{O}} c\mathrm{d}V}{\int_{I+\mathrm{O}} c\mathrm{d}V}. \tag{14}$$

The evolution of the transmission probability obtained by the two methods from $t = 0$ s to $t = 0.01$ s is displayed in Fig. 2 (b). The simulation results are in good agreement with each other, indicating that the Langevin equation in the current work can well reproduce the diffusive behavior of Brownian particles.

We also run a simulation of Brownian particles in turbulent flows based on Eq. (5) and compare the collision rate with the simulation results in Chun and Koch (2005). As shown in Fig. 3, the collision rate has been normalized by the collision kernel of the zero-inertia non-Brownian particles in HIT in Eq. (11). We follow Chun and Koch (2005) and define the particle-scale Peclet number in Fig. 3 as $\mathrm{Pe}_P = \frac{\Gamma_\eta r_p^2}{D}$, where $\Gamma_\eta = u_\eta/\eta$ is the Kolmogorov shear rate. The pure Brownian collision rate and the collision rate for zero-inertia non-Brownian particles in HIT are plotted as solid and dashed lines in Fig. 3. One can see that, as $\mathrm{Pe}_P \to 0$ the collision rate from simulation approaches the pure Brownian collision rate, while turbulence plays the dominant role when $\mathrm{Pe}_P \gg 1$. The consistency between our results and those in Chun and Koch (2005) indicates that the numerical model in the current work can properly capture the effect of both Brownian motion and the turbulence.

3. Results and discussion

In this section, we discuss the results from the DNS-Langevin simulation with different Stokes and Peclet numbers and present the influence of Brownian motion and particle inertia on the radial distribution function (RDF) (Sec. 3.1), the radial relative velocity (Sec. 3.2), and the collision kernel (Sec. 3.3).

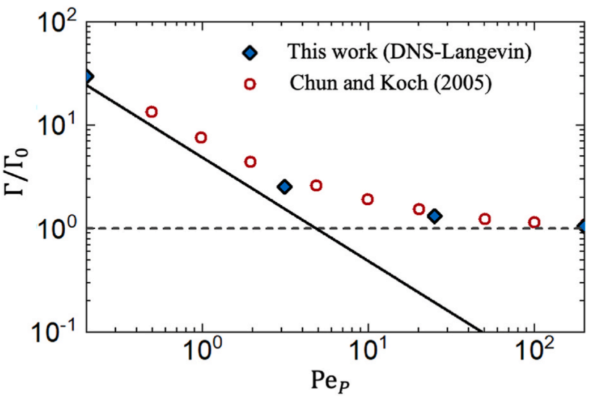

Fig. 3. Collision rate, scaled by the zero-inertia non-Brownian particles in HIT in Eq. (11), as a function of the particle-scale Peclet number. The solid diamonds are results produced by the model in Eq. (5) and the open circles are simulation results in Chun and Koch (2005). The pure Brownian collision rate and the zero-inertia particle collision rate for non-Brownian particles in HIT (Eq. (11)) are plotted as solid and dashed lines, respectively.

3.1. Radial distribution functions

We first present the radial distribution function (RDF) $g(r)$ as a function of the separation distance at different Stokes and Peclet numbers in Fig. 4. The separation distance r of the particle pairs has been scaled by the Kolmogorov length scale η. The influence of the Brownian motion is shown by varying the Peclet number at a fixed Stokes number ($\mathrm{St}_k = 0.112$) (Fig. 4 (a)). A smaller value of Peclet number (i.e., stronger Brownian motion) results in a weaker particle clustering. Such effect is mainly observed within the range of small separation distance r/η. When $r/\eta \gtrsim 1$, $g(r)$ values for different Pe_k numbers are almost the same, the influence of the Brownian motion thus can be neglected. One can also observe that for all Pe_k, the RDF decreases with increasing separation distance and approaches unity at the large separation ($r/\eta \approx 10$). It indicates that the clustering of inertial particles driven by small-scale vortices plays a dominant role in the distribution of particles over the spatial scale $[\eta, 10\eta]$, whereas the Brownian motion can distribute the particles more uniformly with a small length scale $r < \mathrm{O}(\eta)$.

To further quantify the range of the anti-clustering effect of the Brownian motion, we calculate the relative displacement between two Brownian particles in the stationary fluid over the Kolmogorov time scale τ_η. According to the equation of motion of particles in Eq. (5) (neglecting the flow fluctuation), the displacement of a Brownian particle follows the normal distribution $x/\eta \sim N(0, 1/\mathrm{Pe}_k)$ and the relative displacement of two Brownian particles in a direction follows $\Delta x/\eta \sim N(0, 2/\mathrm{Pe}_k)$. The relative displacement of two Brownian particles in the three-dimensional space, $\Delta r = \sqrt{(\Delta x)^2 + (\Delta y)^2 + (\Delta z)^2}$, can be estimated using the root mean square (RMS) of the random variable Δr, which is expressed as

$$\frac{\Delta r_{\mathrm{RMS}}}{\eta} \equiv \frac{\sqrt{\overline{(\Delta r)^2}}}{\eta} = \frac{\sqrt{\overline{(\Delta x)^2} + \overline{(\Delta y)^2} + \overline{(\Delta z)^2}}}{\eta} = \sqrt{\frac{6}{\mathrm{Pe}_k}}. \tag{15}$$

In Fig. 4 (a), the values of $\Delta r_{\mathrm{RMS}}/\eta$ for each case are indicated as vertical dashed lines, which separate the RDFs into two regimes. In the regime of $r/\eta < \sqrt{6/\mathrm{Pe}_k}$, the Brownian motion has a strong anti-clustering effect and the RDF curve is flattened. When $r/\eta > \sqrt{6/\mathrm{Pe}_k}$, the RDF curve begins to decrease and the difference between the curves with different Pe_k values gradually disappears.

The value of RDF at $r/\eta = \sqrt{6/\mathrm{Pe}_k}$ is then noted as g^0 , which reflects the clustering of particles (caused by both Brownian effect and turbulent effect) at small scales. In the inset of Fig. 4 (a), g^0 is plotted as a function of St_k and Pe_k. The value of g^0 decreases with increasing Pe_k^{-1} since the enhanced Brownian motion weakens the clustering of particles at small scales. For a given Pe_k, a larger St_k leads to larger g^0 due to the clustering of particles induced by the particle inertia. The clustering of inertial particles driven by small-scale vortices can be clearly seen in Fig. 4 (b), where the Peclet number is fixed at $\mathrm{Pe}_k = 33.3$ and the Stokes number is varied from 0.022 to 0.112. For very light particles that can follow the fluid faithfully, the clustering effect is weak even for non-Brownian particles. Adding the Brownian random motion to the particles can further inhibit the clustering effect, especially at a small length scale. As the Stokes number increases from 0.022 to 0.112, clustering becomes more significant, which resembles the results for non-Brownian particles (Ray & Collins, 2011; Saw et al., 2008).

The particle distribution, along with the vorticity magnitude, is plotted in Fig. 5 with and without the Brownian motion. The Stokes number is fixed at $\mathrm{St}_k = 0.112$ and the Peclet number is $\mathrm{Pe}_k \to \infty$ in (a) and (d), $\mathrm{Pe}_k = 33.3$ in (b) and (e), and $\mathrm{Pe}_k = 8.33$ in (c) and (f). Plots (d), (e), and (f) are enlarged images from the red box in (a), (b), and (c), respectively. The particles tend to cluster in regions of low vorticity. There is no obvious difference among the three-particle fields when one observes on a large scale. However, when we plot the local enlarged image of a low-vorticity region with a dimension of $\mathrm{O}(\eta)$, the particles with stronger Brownian motion are more sparsely distributed. The observations are in accordance with the results in Fig. 4 that Brownian motion can distribute the particles more uniformly with a small length scale $r < \mathrm{O}(\eta)$.

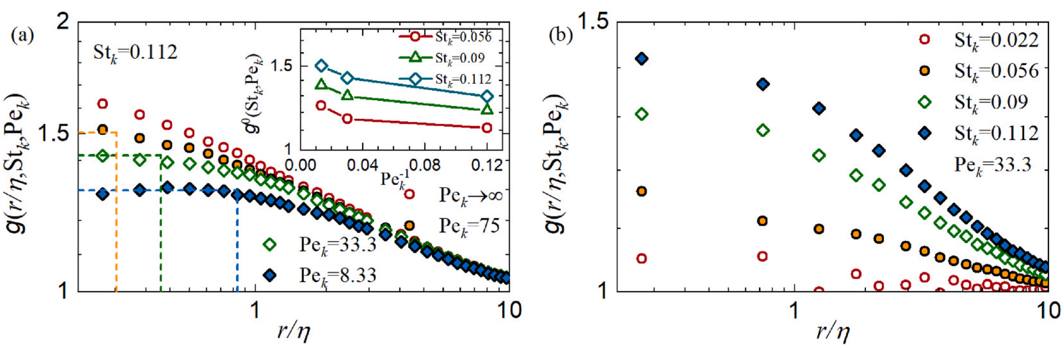

Fig. 4. (a) Radial distribution function (RDF) $g(r/\eta, \mathrm{St}_k, \mathrm{Pe}_k)$ as a function of the scaled separation distance r/η for $\mathrm{Pe}_k \to \infty$ (open circles), $\mathrm{Pe}_k = 75$ (solid circles), 33.3 (open diamonds), and 8.33 (solid diamonds), at $\mathrm{St}_k = 0.112$. The vertical dashed line indicates $r/\eta = \sqrt{6/\mathrm{Pe}_k}$, which separates the non-decreasing and decreasing regimes of the $g(r)$ curve according to Eq. (15). Inset: Variation of g^0 with Pe_k^{-1} for $\mathrm{St}_k = 0.056$ (circles), 0.09 (triangles), and 0.112 (diamonds). (b) RDF as a function of r/η for $\mathrm{St}_k = 0.022$ (open circles), 0.056 (solid circles), 0.09 (open diamonds), and 0.112 (solid diamonds) at $\mathrm{Pe}_k = 33.3$.

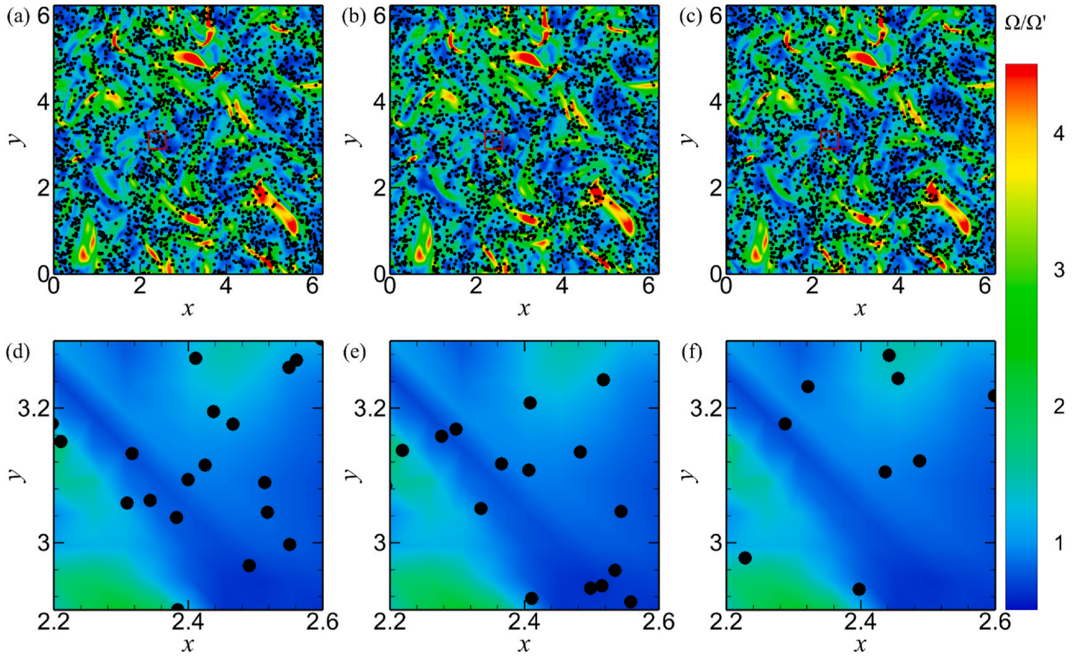

Fig. 5. Particle distribution for $\mathrm{St}_k = 0.112$ and (a, d) $\mathrm{Pe}_k \to \infty$, (b, e) $\mathrm{Pe}_k = 33.3$, and (c, f) $\mathrm{Pe}_k = 8.33$. The particles are superimposed in the vorticity contours in a $240\eta \times 240\eta \times 2\eta$ slice of the flow field. The color codes correspond to vorticity magnitude normalized by the root mean square (RMS) vorticity. (d), (e), and (f) are zoomed-in images of the red box in (a), (b), and (c). (For interpretation of the references to color in this figure legend, the reader is referred to the Web version of this article.)

We then calculate the relative variation of the RDF due to the Brownian motion as follows

$$\Delta\hat{g}(r) = \frac{g(r)_{\mathrm{NB}} - g(r)}{g(r)_{\mathrm{NB}}}, \tag{16}$$

where $g(r)_{\mathrm{NB}}$ is the RDF for non-Brownian particles (i.e. $\mathrm{Pe}_k \to \infty$). The relative variation $\Delta\hat{g}(r)$ at $\mathrm{St}_k = 0.112$ for different Pe_k numbers is shown in Fig. 6. A two-regime behavior can be observed for all three curves. The value of $\Delta\hat{g}(r)$ quickly decreases at small r/η and then remains near zero when r/η is larger than a certain critical value. In the small r/η range, $\Delta\hat{g}(r)$ for larger Pe_k has a larger value and a higher decreasing rate. The value of r/η, when $\Delta\hat{g}(r)$ decreases to 0.01 (indicated by the horizontal dashed line), is regarded as the critical value (termed as r_c^{RDF}/η) separating the two regimes. The critical separation r_c^{RDF}/η indicates the spatial range within which the Brownian motion impacts that particle clustering in the homogeneous isotropic turbulence. When plotted as a function of Pe_k^{-1} (as shown in the inset), r_c^{RDF}/η has a quasi-linear increasing trend.

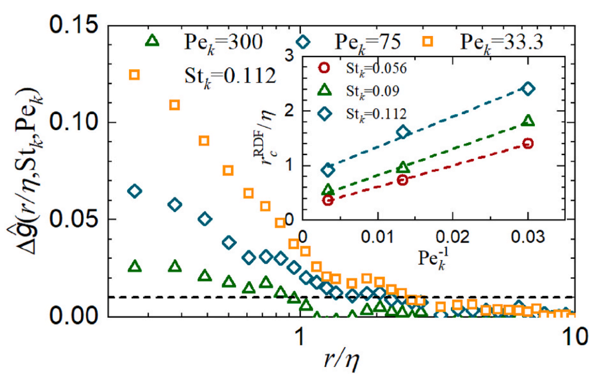

Fig. 6. (a) Relative variation of the RDF $\Delta\hat{g}(r)$ (defined in Eq. (16)) due to the Brownian motion with the scaled separation distance r/η for $\mathrm{Pe}_k =$ 300 (triangles), 75 (diamonds), and 33.33 (squares) at $\mathrm{St}_k = 0.112$. The horizontal dashed line marks $\Delta\hat{g}(r) = 0.01$. Inset: the critical separation distance r_c^{RDF}/η, defined as the distance at which $\Delta\hat{g}(r_c^{\mathrm{RDF}}/\eta) = 0.01$, as a function of the inverse of the Peclet number, Pe_k^{-1}.

3.2. Radial relative velocity

The radial relative velocity (w_r) is another key component that affects the collision rate of particles in the turbulent flow. Here, we calculate the probability density function (PDF) of w_r (scaled by the Kolmogorov velocity scale u_η) at different values of St_k and Pe_k and at a given separation distance ($r/\eta = 0.75$). For non-Brownian particles, PDF does not obviously change when the Stokes number St_k is increased from 0.022 to 0.112 (Fig. 7 (a)). This is due to the small particle inertia of the particles within the given range of the Stokes number. As shown in Fig. 7 (b), when taking the Brownian motion into account ($\mathrm{Pe}_k = 33.3$), a remarkable difference between the PDFs of w_r can be observed within the same range of St_k. Brownian particles with a smaller value of St_k tend to have a larger radial relative velocity. Such a phenomenon can be understood through a velocity superposition analysis (shown below). For a given Stokes number, the variation of PDF curves with Pe_k is presented in Fig. 7 (c). The velocity fluctuation caused by the Brownian motion contributes to the increase of the radial relative velocity, leading to a wider PDF curve of w_r.

The radial relative velocity is supposed to be a linear superposition of the radial relative velocity caused by turbulence effect and Brownian motion, and we assume that the radial relative velocity of Brownian particles in the homogeneous isotropic turbulent flow can be obtained by adding a random velocity component caused by Brownian fluctuation to the radial relative velocity of non-Brownian particles with the same Stokes number. This velocity superposition analysis can be written as

$$\frac{w_r(\mathrm{St}_k, \mathrm{Pe}_k)}{u_\eta} = \frac{w_r(\mathrm{St}_k, \mathrm{Pe}_k = \infty)}{u_\eta} + \widehat{\omega}_r^{\mathrm{ST}}(\mathrm{St}_k, \mathrm{Pe}_k) \tag{17}$$

where $\widehat{\omega}_r^{\mathrm{ST}}(\mathrm{St}_k, \mathrm{Pe}_k)$ is a random variable that follows the normal distribution $\mathscr{N}(0, (\mathrm{St}_k\mathrm{Pe}_k)^{-1})$ reflecting the Brownian effect on the relative motion, and $w_r(\mathrm{St}_k, \mathrm{Pe}_k = \infty)$ represents the turbulence effect on the radial relative velocity. The derivation and validation of the normal distribution for $\widehat{\omega}_r^{\mathrm{ST}}(\mathrm{St}_k, \mathrm{Pe}_k)$ is shown in Appendix A. In Fig. 8, we compare the PDF of w_r/u_η that is calculated from Eq. (17) (shown as lines) with those calculated from DNS simulations (shown as symbols). A good agreement between the two data sets can be observed, indicating that once we know the PDF of w_r/u_η of non-Brownian particles in HIT, the PDF of Brownian particles with the same St_k but different Pe_k values can be easily obtained from Eq. (17).

We then discuss how the PDF of relative radial relative velocity $w_r(r)$ and the mean radial inward velocity $\langle w_r \rangle^{(-)}$ vary with the interparticle separation r. The mean radial inward velocity at a given separation r is calculated as (de Jong et al., 2010):

$$\langle w_r \rangle^{(-)} = \int_{-\infty}^{0} -w_r(r)P(w_r|r)\mathrm{d}w_r. \tag{18}$$

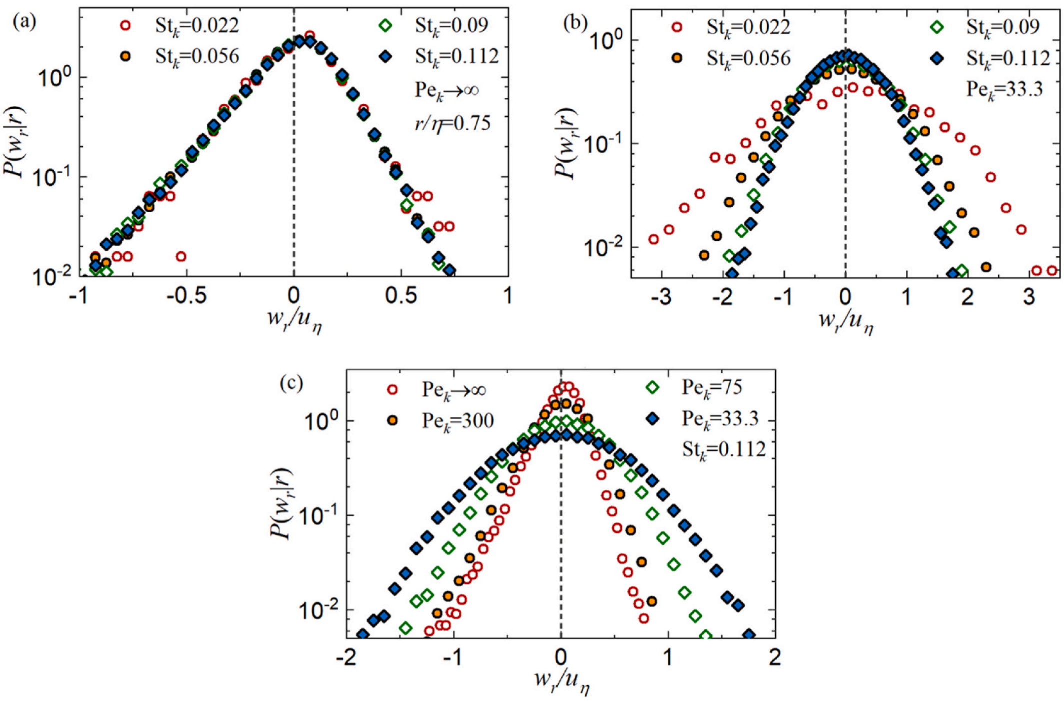

Fig. 7. Probability density function (PDF) of the radial relative velocity $w_r(r)$ (scaled by the Kolmogorov velocity u_η) at the separation distance $r/\eta = 0.75$ for $\mathrm{St}_k = 0.022$ (open circles), 0.056 (solid circles), 0.09 (open diamonds), and 0.112 (solid diamonds) with (a) $\mathrm{Pe}_k \to \infty$ (non-Brownian particles) and (b) $\mathrm{Pe}_k = 33.3$. (c) PDF of $w_r(r)/u_\eta$ at $r/\eta = 0.75$, and 33.3 (solid diamonds) at $\mathrm{St}_k = 0.112$.

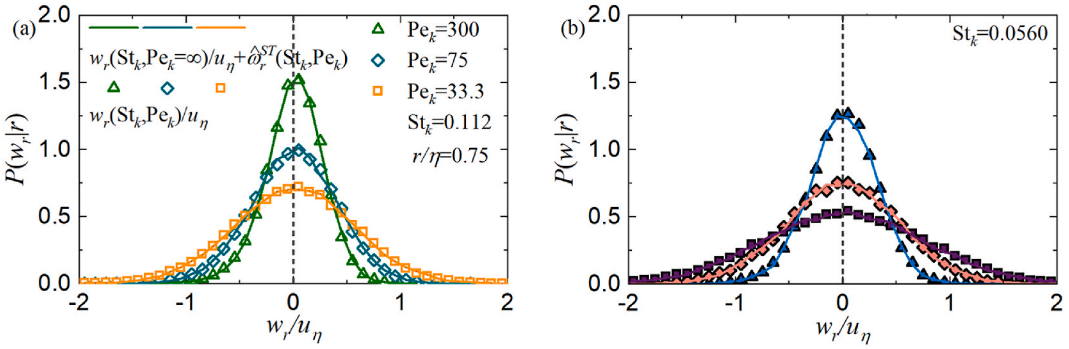

Fig. 8. Probability density function of the radial relative velocity $w_r(r)$ (scaled by the Kolmogorov velocity u_η) at $r/\eta = 0.75$ from simulation results (symbols) for $\mathrm{Pe}_k = 300$ (triangles), 75 (diamonds), and 33.3 (squares) and obtained by the velocity superposition analysis in Eq. (17) (shown as lines). Panels (a) and (b) are results for $\mathrm{St}_k = 0.112$ and 0.056, respectively.

In Fig. 9 (a), the $\langle w_r\rangle^{(-)}/u_\eta$ is plotted as a function of the scaled separation distance r/η for different values of Pe_k at $\mathrm{St}_k = 0.112$. As r/η decreases, there will be a stronger correlation between the velocity of a pair of particles, leading to a decrease of $\langle w_r\rangle^{(-)}/u_\eta$. For non-Brownian particles ($\mathrm{Pe}_k \to \infty$) with negligible inertia, the radial inward velocity is essentially zero at the limit $r/\eta \to 0$ since the two particles follow the streamline at the same position. Due to the random velocity of the Brownian motion, $\langle w_r\rangle^{(-)}$ at the zero separation limit is non-zero and increases with the decrease of Pe_k. $\langle w_r\rangle^{(-)}$ at $r/\eta \to 0$ can be well estimated using the PDF of $w_r(r)$ of Brownian particles in the stationary fluid (shown as dashed lines in Fig. 9 (a)). At a large separation distance (say, $r/\eta = 10$), the radial relative velocity $w_r(r)$ is mainly caused by the fluid velocity difference at the position of the two particles. The difference between the values of $\langle w_r\rangle^{(-)}$ for different values of Pe_k, therefore, is no longer obvious.

The relative increase of the mean radial inward velocity of Brownian particles with respect to that of non-Brownian particles (termed as $\langle w_r\rangle^{(-)}_{\mathrm{NB}}$) is calculated as $\Delta\langle w_r\rangle^{(-)}/\langle w_r\rangle^{(-)}_{\mathrm{NB}} \equiv (\langle w_r\rangle^{(-)} - \langle w_r\rangle^{(-)}_{\mathrm{NB}})/\langle w_r\rangle^{(-)}_{\mathrm{NB}}$ and is plotted as a function of the separation distance in Fig. 9 (b). When $r/\eta < 1$, $\Delta\langle w_r\rangle^{(-)}/\langle w_r\rangle^{(-)}_{\mathrm{NB}}$ decreases with r/η and the curve with a larger value of Pe_k has a higher decreasing rate. As r/η increases, the increment of the mean radial inward velocity $\Delta\langle w_r\rangle^{(-)}$ decreases whereas the mean radial inward velocity due to the non-uniform flow velocity $\langle w_r\rangle^{(-)}_{\mathrm{NB}}$ increases, which leads to the decrease of $\Delta\langle w_r\rangle^{(-)}/\langle w_r\rangle^{(-)}_{\mathrm{NB}}$. When r/η is sufficiently large, $\Delta\langle w_r\rangle^{(-)}/\langle w_r\rangle^{(-)}_{\mathrm{NB}}$ is close to zero implying that the role of Brownian motion on particle relative velocity can be neglected at a large length scale. In the inset of Fig. 9 (b), the critical separation r_c^{RRV}/η, which is defined as the distance when $\Delta\langle w_r\rangle^{(-)}/\langle w_r\rangle^{(-)}_{\mathrm{NB}}$ decreases to 0.1, is plotted as a function of Pe_k^{-1}. The value of r_c^{RRV}/η almost increases linearly with the inverse of the Peclet number. The trend of r_c^{RRV}/η is similar to that of the critical separation of the radial distribution function, r_c^{RDF}/η, as shown in Fig. 6.

3.3. Estimation of collision kernel

In this section, we use RDF and the distribution of the radial relative velocity to construct the collision kernel for Brownian par-

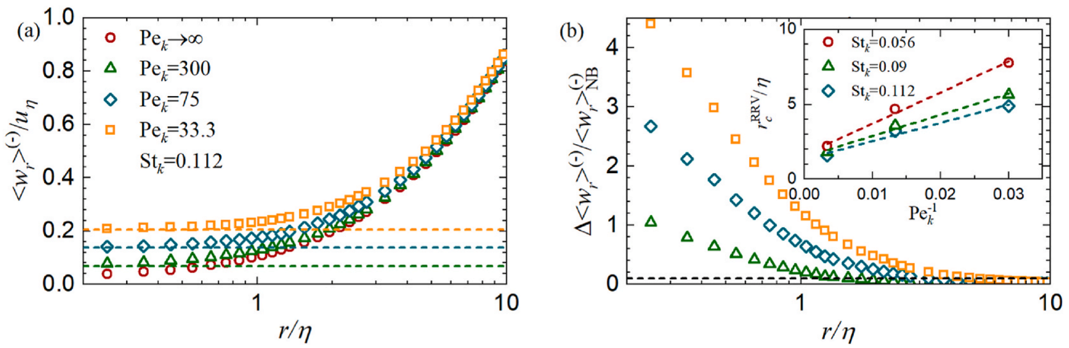

Fig. 9. (a) Variation of the mean radial inward velocity $\langle w_r\rangle^{(-)}$, scaled by Kolmogorov velocity u_η, with the scaled separation distance r/η for $\mathrm{Pe}_k \to \infty$ (circles), $\mathrm{Pe}_k = 300$ (triangles), 75 (diamonds), and 33.3 (squares) at $\mathrm{St}_k = 0.112$. The horizontal dashed lines indicate the mean radial inward velocities of Brownian particles in the stationary fluid. (b) The ratio between the variation of the mean radial inward velocity differences $\Delta\langle w_r\rangle^{(-)}$, scaled by the mean radial inward velocity without Brownian motion $\langle w_r\rangle^{(-)}_{\mathrm{NB}}$, as a function of the scaled separation distance r/η. The legends are the same as those in (a). Inset: variation of the critical separation distance r_c^{RRV}/η with Pe_k^{-1} for $\mathrm{St}_k = 0.056$ (circles), 0.09 (triangles), and 0.112 (diamonds).

ticles. As shown in Table 1, the particle diameter is smaller than the Kolmogorov length scale by four orders of magnitude. The statistics for the collision rate, the radial distribution function, and the radial relative velocity at such a small separation are not available. Therefore, we model the geometric collision kernel (Ayala et al., 2008) for particles at the separation $r \sim O(\eta)$ using Eq. (10) (Sundaram & Collins, 1997) and look at how $\Gamma(r)$ varies with r when r approaches zero.

In Fig. 10, the modeled geometric collision kernel, scaled by the kernel for inertialess non-Brownian particles Γ_0, is plotted as a function of the collision distance r. Due to the small value of St_k, Γ/Γ_0 for particles without Brownian motion is close to unity and only slightly increases as St_k increases from 0.022 to 0.112. Introducing the Brownian motion ($\mathrm{Pe}_k = 33.3$) significantly increases the geometric collision kernel, especially at a small separation. At this value of Pe_k, particles with a smaller St_k have a larger geometric collision kernel. According to the results in Fig. 7 (b), given a fixed value of Pe_k, particles with a smaller Stokes number tend to have a larger radial relative velocity, which results in a higher value of Γ/Γ_0. The influence of the intensity of the Brownian motion (Pe_k) on the geometric collision kernel is presented in Fig. 10 (b). One can see that the Brownian motion promotes particle collision, especially at the sub-Kolmogorov scale. Despite that the anti-clustering effect of the Brownian motion gives rise to a smaller value of $g(r)$, the increased radial relative velocity counteracts the anti-clustering effect on the geometric collision kernel and leads to a larger value of Γ/Γ_0.

We then discuss how the geometric collision kernel scales with the collision radius, r/η, when r/η approaches zero. According to the results in Fig. 4, when the Brownian motion is strong, the radial distribution function approaches an asymptotic value, i.e., $g(\mathrm{St}_k,\mathrm{Pe}_k, r/\eta) \to g^0(\mathrm{St}_k,\mathrm{Pe}_k)$, at the small separation limit ($r/\eta \to 0$). The mean radial inward velocity $\langle w_r\rangle^{(-)}/u_\eta$ can be well estimated using the PDF of $w_r(r)$ of Brownian particles in the stationary fluid (Eq. (17)) and is expressed as

$$\frac{\langle w_r\rangle^{(-)}}{u_\eta} \approx \frac{1}{\sqrt{2\pi\cdot\mathrm{St}_k\cdot\mathrm{Pe}_k}}, \text{ when } r/\eta \to 0. \tag{19}$$

Substituting $g(r)$ and $\int_{-\infty}^{0} -w_r(r)P(w_r|r)\mathrm{d}w_r$ into Eq. (10) with the corresponding asymptotic values and Γ_0 with $\sqrt{\frac{8\pi}{15}}r^3\frac{u_\eta}{\eta}$ (Saffman & Turner, 1956), we have

$$\Gamma/\Gamma_0 \approx \frac{\sqrt{15}g^0}{\sqrt{\mathrm{St}_k\cdot\mathrm{Pe}_k}}\left(\frac{r}{\eta}\right)^{-1} \text{ when } r/\eta \to 0. \tag{20}$$

To verify the asymptotic value of Γ/Γ_0 at the small collision distance limit, we calculate the value of Γ/Γ_0 by adopting three different methods. (i) Γ is calculated according to Eq. (8), where the collision rate is obtained from DNS simulation. The geometric collision kernel determined in this way is numerical results and is termed as Γ^{DNS}. (ii) The geometric collision kernel Γ is modeled according to Eq. (10), in which the RDF $g(r)$ and the PDF of RRV are fitted from DNS results. The geometric collision kernel calculated in this way is termed as Γ^{EST1}. (iii) Γ is calculated according to Eq. (20), where g^0 is the asymptotic value of $g(r)$ at the small r/η limit (calculated at $r/\eta = \sqrt{6/\mathrm{Pe}_k}$ according to Eq. (15)). The geometric collision kernel calculated in this way is recorded as Γ^{EST2}. In the first method, the collision number recorded is at least 4×10^3 to ensure reasonable statistics and the overall simulation time is long enough to ensure that the geometric collision kernel has reached its steady-state value.

The geometric collision kernel, Γ/Γ_0, calculated in these three ways are shown in Fig. 11 as open symbols, solid symbols, and dashed lines, respectively. Here, the Stokes number is $\mathrm{St}_k = 0.112$ and the Peclet number is varied from 3.0 to 75. One can see that Γ/Γ_0 values given by the three ways are quite close to each other. It implies that the collision kernel for Brownian particles, whose size is much smaller than the Kolmogorov scale ($d_p \ll \eta$), can be well predicted using Eq. (20). When the Brownian motion is strong, the parameters in Eq. (20) are either known a priori (such as St_k, Pe_k, and η) or can be calculated from DNS at a finite collision distance ($r/\eta \sim \sqrt{6/\mathrm{Pe}_k}$) (recall that $g(r/\eta) \to g^0$ at a finite value of r/η when Pe_k is relatively small). Since there are obvious asymptotic behaviors of radial distribution function and radial relative velocity at the small separation, and the collision events are determined by

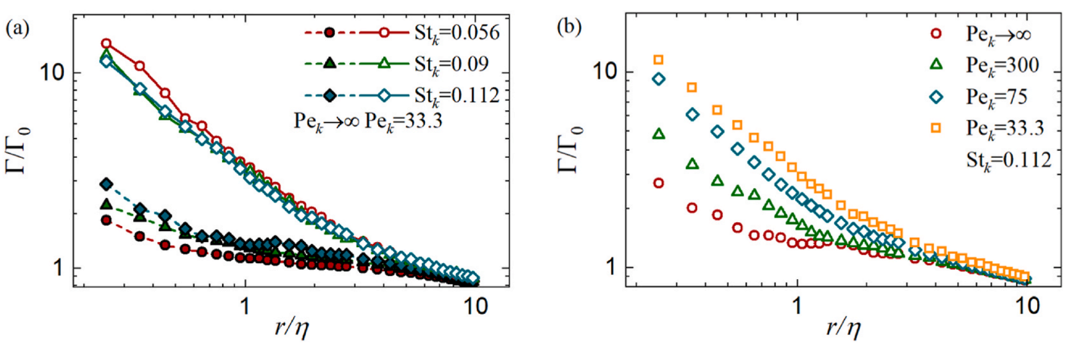

Fig. 10. (a) Variation of the modeled geometric collision kernel Γ (Eq. (10)), scaled by the collision kernel of inertialess particles Γ_0, as a function of the collision distance r/η for $\mathrm{St}_k = 0.056$ (circles), 0.09 (triangles), and 0.112 (diamonds) at $\mathrm{Pe}_k \to \infty$ (solid symbols) and $\mathrm{Pe}_k = 33.3$ (open symbols). (b) Scaled geometric collision kernel Γ/Γ_0 for $\mathrm{Pe}_k \to \infty$ (circles), $\mathrm{Pe}_k = 300$ (triangles), 75 (diamonds), and 33.3 (squares) and $\mathrm{St}_k = 0.112$.

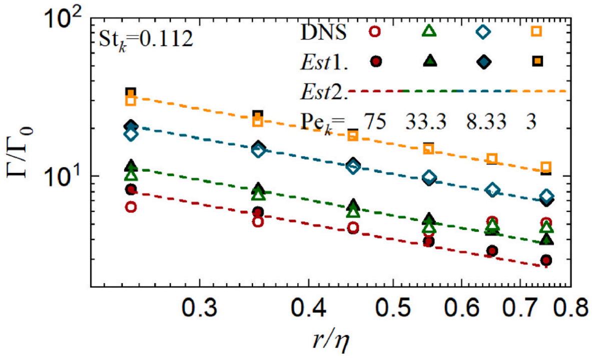

Fig. 11. Geometric collision kernel, Γ/Γ_0, as a function of the collision radius r/η, for particles with Peclet number $\mathrm{Pe}_k = 75$ (circles), 33.3 (triangles), 8.33 (diamonds), and 3.0 (squares) and $\mathrm{St}_k = 0.112$. Here, Γ_0 is the collision kernel for zero-inertia particles (Saffman & Turner, 1956). The open symbols are results given by counting the collision number in DNS simulations ($\Gamma^{\mathrm{DNS}}/\Gamma_0$). Solid symbols are results modeled according to Eq. (10) using the radial distribution function $g(r)$ and the mean radial inward velocity $\langle w_r\rangle^{(-)}$ ($\Gamma^{\mathrm{Est1}}/\Gamma_0$). Dashed lines are results predicted from the asymptotic values of $g(r)$ and $\langle w_r\rangle^{(-)}$ according to Eq. (20) ($\Gamma^{\mathrm{Est2}}/\Gamma_0$).

the collision geometry, the particle distribution, and particle velocities according to Eq. (10), it is a reasonable to estimate the real collision kernel at $r = d_p$ by extrapolating the geometric collision kernel with asymptotic values. However, detailed experimental validation is required in future.

It is of interest to compare the collision kernel in Eq. (20) with the Brownian collision kernel for particles with a diameter much smaller than the gas mean free path, which is expressed as (Friedlander, 2000)

$$\Gamma(v_i, v_j) = \left(\frac{3}{4\pi}\right)^{\frac{1}{6}}\left(\frac{6k_BT}{\rho_p}\right)^{\frac{1}{2}}\left(\frac{1}{v_i}+\frac{1}{v_j}\right)^{\frac{1}{2}}\left(v_i^{\frac{1}{3}}+v_j^{\frac{1}{3}}\right)^2. \tag{21}$$

Here, v_i is the volume of particle i. For monodisperse particles, the collision kernel scaled by the collision kernel of the zero-inertia particles in homogenous isotropic turbulence Γ_0 takes the form

$$\Gamma/\Gamma_0 = \frac{\sqrt{15}}{\sqrt{\mathrm{St}_k\cdot\mathrm{Pe}_k}}\left(\frac{d_p}{\eta}\right)^{-1}. \tag{22}$$

One can see that the difference is the radial distribution function g^0, which reflects the inhomogeneous particle distribution caused by the turbulence. The difference between Eq. (20) and Eq. (22) highlights the feature brought out by turbulence.

4. Conclusions

In this work, the clustering and collision of Brownian particles in homogeneous isotropic turbulence are investigated using DNS and the Langevin dynamics. We have calculated the radial distribution function (RDF), $g(r)$, and the radial relative velocity (RRV), $w_r(r)$, for particles with different inertia ($\mathrm{St}_k = 0.022 \sim 0.112$) and Brownian motion intensity ($\mathrm{Pe}_k = 3.0 \sim \infty$). We find that the Brownian motion can distribute the particles more uniformly over a small spatial range, leading to the formation of a plateau on the $g(r)$ curve at a small separation r. The range of r , where the plateau of the $g(r)$ curve appears, can be estimated by the root mean square value of the relative displacement between two Brownian particles over the Kolmogorov time scale τ_η. The anti-clustering effect of the Brownian motion is then quantified by the relative variation of the RDF, $\Delta\widehat{g}(r)$, which quickly decreases at small r/η and then remains near zero when r/η is larger than a certain critical value.

The radial relative velocity is significantly enhanced, especially at the small separation distance, when the Brownian motion is taken into account. A velocity superposition analysis shows that the statistics of w_r of Brownian particles can be obtained by adding a random variable $\widehat{\omega}_r^{\mathrm{ST}}$ onto the radial relative velocity of non-Brownian particles with the same Stokes number. Here, $\widehat{\omega}_r^{\mathrm{ST}}$ is a random variable that describes the radial relative velocity of two Brownian particles in the stationary fluid and follows the normal distribution $\mathcal{N}(0, (\mathrm{St}_k\mathrm{Pe}_k)^{-1})$.

The geometric collision kernel ($\Gamma(r)$) for particles at the separation $r \sim \mathrm{O}(\eta)$ is then calculated. Despite that the Brownian motion gives rise to a smaller value of $g(r)$, the increased radial relative velocity counteracts the anti-clustering effect on the geometric collision kernel and leads to a larger value of $\Gamma(r)$. We then proposed an analytical expression for the mean radial inward velocity $\langle w_r\rangle^{(-)}$ at the small separation limit ($r/\eta \to 0$). Based on the asymptotic values of $\langle w_r\rangle^{(-)}$ and RDF $g(r)$, we can predict the collision kernel of Brownian particles at a vanishing interparticle separation distance. The current work focuses on the collision rate of monodisperse nanoparticles, which is relevant in the early stage of the agglomeration process. The following growth of the agglomerates is strongly influenced by the clustering and collision between agglomerates in turbulence (Njobuenwu & Fairweather, 2018). An accurate simulation of the motion of nanosized agglomerates (for example, using DNS-Langevin dynamics) requires the knowledge of hydrodynamic forces on agglomerates with irregular shapes (Chen et al., 2022; Qian et al., 2022). The growth rate, size, and structural evolution of agglomerates under the turbulent transport and Brownian motion will be investigated in the future.

Declaration of competing interest

The authors declare that they have no known competing financial interests or personal relationships that could have appeared to influence the work reported in this paper.

Data availability

Data will be made available on request.

Acknowledgments

We acknowledge support from the National Natural Science Foundation of China (Grant No. 52006084 and 52130606). The authors would like to thank Professor Minghou Xu at Huazhong University of Science and Technology and Prof. Yiyang Zhang at Tsinghua University for fruitful discussion.

Appendix

A. Derivation and validation of Brownian radial relative velocity

The Brownian fluctuation on radial relative velocity can be obtained by calculating the velocity distributions of Brownian particles with different combinations of St_k and Pe_k in a virtual stationary fluid. This can be simply done by setting the fluid velocity in Eq. (5) to zero ($\widehat{\boldsymbol{u}}_f = 0$). The radial relative velocity of Brownian particles in the stationary fluid (termed as w_r^{ST}) is calculated and the PDF of w_r^{ST} is constructed, shown in Fig. A1(a) for two Stokes numbers ($\mathrm{St}_k = 0.11$ and 0.056) and three Peclet numbers ($\mathrm{Pe}_k = 300$, 75, and 33.3). For a better comparison between the radial relative velocity of Brownian particles w_r^{ST} with that caused by the turbulence, we still use the Kolmogorov scales to normalize the quantities of Brownian particles in the stationary fluid. The normalization process introduces the parameters Pe_k and St_k. It is straightforward that particles with a stronger Brownian motion tend to have a wider PDF of w_r^{ST}. Reducing particle inertia also helps to increase the radial relative velocity. The radial relative velocity and the PDF are then standardized according to

$$\left(w_r^{\mathrm{ST}}/u_\eta\right)^* = \frac{w_r^{\mathrm{ST}}/u_\eta}{\sigma_{\mathrm{ST}}}, \tag{23a}$$

$$P^*\left(\left(w_r^{\mathrm{ST}}/u_\eta\right)^*\right) = P\left(w_r^{\mathrm{ST}}/u_\eta\right)\cdot\sigma_{\mathrm{ST}}. \tag{23b}$$

Here, σ_{ST} is the standard deviation of the scaled radial relative velocity w_r^{ST}/u_η. As shown in Fig. A1 (b), the standardized PDF for all the six cases in Fig. A1 (a) well follows the standard normal distribution $\mathcal{N}(0,1)$. Consequently, σ_{ST} becomes the only parameter that determines the PDF of w_r^{ST}/u_η of Brownian particles in the stationary fluid.

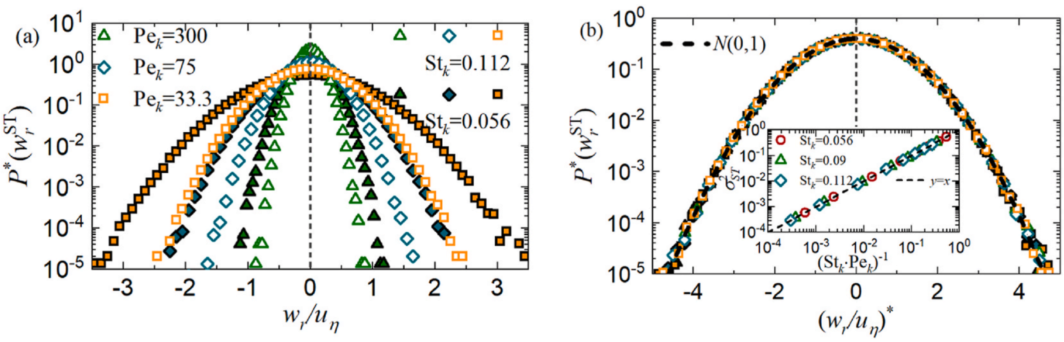

Fig. A.1. (a) Probability density function of the relative radial velocity $w_r^{\mathrm{ST}}(r)$ (scaled by the Kolmogorov velocity u_η) for Brownian particles in the stationary fluid with $\mathrm{St}_k = 0.056$ (open symbols) and 0.112 (solid symbols) and $\mathrm{Pe}_k = 300$ (triangles), 75 (diamonds), and 33.3 (squares). (b) Standardized PDF of the radial relative velocity $\left(w_r^{\mathrm{ST}}/u_\eta\right)^* \equiv \frac{w_r^{\mathrm{ST}}/u_\eta}{\sigma_{ST}}$ for the same cases as those in (a). The black dashed line stands for the standard normal distribution $\mathcal{N}(0,1)$. In the inset of (b), the squared standard deviation σ_{ST}^2 is compared with $(\mathrm{St}_k\mathrm{Pe}_k)^{-1}$ and the dashed line indicates $\sigma_{\mathrm{ST}}^2 = (\mathrm{St}_k\mathrm{Pe}_k)^{-1}$.

From Eq. (5), one can derive that the velocity component in each direction, u_x/u_η, of Brownian particles in the stationary fluid follows the normal distribution $\mathcal{N}\left(0, \frac{1}{2\mathrm{St}_k\mathrm{Pe}_k}\right)$. The distribution of the relative velocity between two particles in a given direction, $\Delta u_x / u_\eta = (u_{i,x} - u_{j,x}) / u_\eta$, thus is also a normal distribution $\mathcal{N}\left(0, \frac{1}{\mathrm{St}_k\mathrm{Pe}_k}\right)$. The magnitude of the relative velocity between two particles, $\Delta U / u_\eta = \sqrt{\Delta u_x^2 + \Delta u_y^2 + \Delta u_z^2} / u_\eta$, follows the Maxwell-Boltzmann distribution

$$P_{\Delta U/u_\eta}(\Delta U / u_\eta) = \sqrt{\frac{2}{\pi}}\ \frac{(\Delta U/u_\eta)^2}{a^3}\exp\left(-\frac{(\Delta U/u_\eta)^2}{2a^2}\right), \tag{24}$$

where the parameter $a = (\mathrm{St}_k\mathrm{Pe}_k)^{-\frac{1}{2}}$. The distribution of the radial relative velocity can be calculated from the distribution of the relative velocity ΔU and the distribution of $\cos\theta$, with θ being the angle between the relative velocity and the line connecting the center of the two particles. It gives

$$P\left(\frac{w_r^{\mathrm{ST}}}{u_\eta}\right) = \frac{1}{\sqrt{2\pi}a}\exp\left(-\frac{\left(w_r^{\mathrm{ST}}/u_\eta\right)^2}{2a^2}\right), \tag{25}$$

which implies that the radial relative velocity of Brownian particle in the stationary fluid should follow the normal distribution of $\mathcal{N}(0, (\mathrm{St}_k\mathrm{Pe}_k)^{-1})$. The squared standard deviation σ_{ST}^2 produced by the simulation of Brownian particles in the stationary fluid is compared with $(\mathrm{St}_k\mathrm{Pe}_k)^{-1}$ in the inset of Fig. A1 (b). All the data points collapse onto the curve of $\sigma_{\mathrm{ST}}^2 = (\mathrm{St}_k\mathrm{Pe}_k)^{-1}$, which is in accordance with the analytical expression in Eq. (25).

References

Ayala, O., Rosa, B., Wang, L. P., & Grabowski, W. W. (2008). Effects of turbulence on the geometric collision rate of sedimenting droplets. Part 1. Results from direct numerical simulation. *New Journal of Physics, 10*(7), Article 075015.
Balachandar, S., & Eaton, J. K. (2010). Turbulent dispersed multiphase flow. *Annual Review of Fluid Mechanics, 42*, 111–133.
Bec, J., Musacchio, S., & Ray, S. S. (2013). Sticky elastic collisions. *Physical Review E, 87*(6), Article 063013.
Boje, A., & Kraft, M. (2022). Stochastic population balance methods for detailed modelling of flame-made aerosol particles. *Journal of Aerosol Science, 159*, Article 105895.
Bringley, E. J., Manuputty, M. Y., Lindberg, C. S., Leon, G., Akroyd, J., & Kraft, M. (2022). Simulations of TiO2 nanoparticles synthesised off-centreline in jet-wall stagnation flames. *Journal of Aerosol Science*, Article 105928.
Buckley, R. L., & Loyalka, S. K. (1989). Cunningham correction factor and accommodation coefficient: Interpretation of millikan's data. *Journal of Aerosol Science, 20*(3), 347–349.
Camenzind, A., Schulz, H., Teleki, A., Beaucage, G., Narayanan, T., & Pratsinis, S. E. (2008). Nanostructure evolution: From aggregated to spherical SiO2 particles made in diffusion flames. *European Journal of Inorganic Chemistry*, 911–918, 2008.
Chen, S., Chen, P., & Fu, J. (2022). Drag and lift forces acting on linear and irregular agglomerates formed by spherical particles. *Physics of Fluids, 34*(2), Article 023307.
Chen, S., Cheng, M., Xu, J., Liu, X., Yu, D., & Xu, M. (2021). Numerical analysis on reduction of ultrafine particulate matter by a kaolin additive during pulverized coal combustion. *Energy & Fuels, 35*(11), 9538–9549.
Chen, S., & Li, S. (2020). Collision-induced breakage of agglomerates in homogenous isotropic turbulence laden with adhesive particles. *Journal of Fluid Mechanics*902.
Chen, S., Li, S., & Marshall, J. S. (2019). Exponential scaling in early-stage agglomeration of adhesive particles in turbulence. *Physical Review Fluids, 4*(2), Article 024304.
Chen, S., Liu, W., & Li, S. (2016). Effect of long-range electrostatic repulsion on pore clogging during microfiltration. *Physical Review E, 94*(6), Article 063108.
Choi, H., Kang, S., Jung, W., Jung, Y. H., Park, S. J., Kim, D. S., & Choi, M. (2015). Controlled electrostatic focusing of charged aerosol nanoparticles via an electrified mask. *Journal of Aerosol Science, 88*, 90–97.
Chumakov, S. G. (2006). Statistics of subgrid-scale stress states in homogeneous isotropic turbulence. *Journal of Fluid Mechanics, 562*, 405–414.
Chun, J., & Koch, D. L. (2005). Coagulation of monodisperse aerosol particles by isotropic turbulence. *Physics of Fluids, 17*(2), Article 027102.
Cifuentes, L., Sellmann, J., Wlokas, I., & Kempf, A. (2020). Direct numerical simulations of nanoparticle formation in premixed and non-premixed flame–vortex interactions. *Physics of Fluids, 32*(9), Article 093605.
De Jong, J., Salazar, J. P. L. C., Woodward, S. H., Collins, L. R., & Meng, H. (2010). Measurement of inertial particle clustering and relative velocity statistics in isotropic turbulence using holographic imaging. *International Journal of Multiphase Flow, 36*(4), 324–332.
Dizaji, F. F., & Marshall, J. S. (2016). An accelerated stochastic vortex structure method for particle collision and agglomeration in homogeneous turbulence. *Physics of Fluids, 28*(11), Article 113301.
Dizaji, F. F., Marshall, J. S., & Grant, J. R. (2018). A stochastic vortex structure method for interacting particles in turbulent shear flows. *Physics of Fluids, 30*(1), Article 013301.
Endres, S. C., Ciacchi, L. C., & Mädler, L. (2021). A review of contact force models between nanoparticles in agglomerates, aggregates, and films. *Journal of Aerosol Science, 153*, Article 105719.
Epstein, P. S. (1924). On the resistance experienced by spheres in their motion through gases. *Physical Review, 23*(6), 710.
Falkovich, G., Fouxon, A., & Stepanov, M. G. (2002). Acceleration of rain initiation by cloud turbulence. *Nature, 419*(6903), 151–154.
Fayed, H. E., & Ragab, S. A. (2013). Direct numerical simulation of particles-bubbles collisions kernel in homogeneous isotropic turbulence. *The Journal of Computational Multiphase Flows, 5*(3), 167–188.
Friedlander, S. K. (2000). *Smoke, dust, and haze*. New York: Oxford University Press.
Fuchs, N. A. (1964). *The mechanics of aerosols*. New York: Pergamon Press.
Garrick, S. C. (2011). Effects of turbulent fluctuations on nanoparticle coagulation in shear flows. *Aerosol Science and Technology, 45*(10), 1272–1285.
Glassman, I., & Yetter, R. A. (2008). *Combustion* (4th ed.). Burlington, Vermont: Academic Press.
Gspann, T. S., Juckes, S. M., Niven, J. F., Johnson, M. B., Elliott, J. A., White, M. A., & Windle, A. H. (2017). High thermal conductivities of carbon nanotube films and micro-fibres and their dependence on morphology. *Carbon, 114*, 160–168.
Gustavsson, K., & Mehlig, B. (2016). Statistical model for collisions and recollisions of inertial particles in mixing flows. *The European Physical Journal E, 39*(5), 1–9.
Heine, M. C., & Pratsinis, S. E. (2007). Brownian coagulation at high concentration. *Langmuir, 23*(19), 9882–9890.

Hitimana, E., Fox, R. O., Hill, J. C., & Olsen, M. G. (2021). Coherent structure characteristics of the swirling flow during turbulent mixing in a multi-inlet vortex reactor. *Physics of Fluids, 33*(6), Article 065119.
Hou, D., Zong, D., Lindberg, C. S., Kraft, M., & You, X. (2020). On the coagulation efficiency of carbonaceous nanoparticles. *Journal of Aerosol Science, 140*, Article 105478.
Huang, Q., Li, S., Li, G., & Yao, Q. (2017). Mechanisms on the size partitioning of sodium in particulate matter from pulverized coal combustion. *Combustion and Flame, 182*, 313–323.
Inci, G., Kronenburg, A., Weeber, R., & Pflüger, D. (2017). Langevin dynamics simulation of transport and aggregation of soot nano-particles in turbulent flows. *Flow, Turbulence and Combustion, 98*(4), 1065–1085.
Janzen, C., & Roth, P. (2001). Formation and characteristics of Fe2O3 nano-particles in doped low pressure H2/O2/Ar flames. *Combustion and Flame, 125*(3), 1150–1161.
Jaworek, A., Marchewicz, A., Sobczyk, A. T., Krupa, A., & Czech, T. (2018). Two-stage electrostatic precipitators for the reduction of PM2. 5 particle emission. *Progress in Energy and Combustion Science, 67*, 206–233.
Jiang, L., Rahnama, M., Zhang, B., Zhu, X., Sui, P. C., Ye, D. D., & Djilali, N. (2020). Predicting the interaction between nanoparticles in shear flow using lattice Boltzmann method and Derjaguin–Landau–Verwey–Overbeek (DLVO) theory. *Physics of Fluids, 32*(4), Article 043302.
Kellogg, K. M., Liu, P., LaMarche, C. Q., & Hrenya, C. M. (2017). Continuum theory for rapid cohesive-particle flows: General balance equations and discrete-element-method-based closure of cohesion-specific quantities. *Journal of Fluid Mechanics, 832*, 345–382.
Langevin, P. (1908). Sur la théorie du mouvemenovementn. *Compt. Rendus, 146*, 530–533.
Li, A., & Ahmadi, G. (1992). Dispersion and deposition of spherical particles from point sources in a turbulent channel flow. *Aerosol Science and Technology, 16*(4), 209–226.
Lian, H., Chang, X. Y., & Hardalupas, Y. (2019). Time resolved measurements of droplet preferential concentration in homogeneous isotropic turbulence without mean flow. *Physics of Fluids, 31*(2), Article 025103.
Li, L., & Gopalakrishnan, R. (2021). An experimentally validated model of diffusion charging of arbitrary shaped aerosol particles. *Journal of Aerosol Science, 151*, Article 105678.
Li, S. Q., & Marshall, J. S. (2007). Discrete element simulation of micro-particle deposition on a cylindrical fiber in an array. *Journal of Aerosol Science, 38*(10), 1031–1046.
Lindackers, D., Strecker, M. G. D., Roth, P., Janzen, C., & Pratsinis, S. E. (1997). Formation and growth of SiO2 particlesin low pressure H2/O2/Ar flames doped with SiH4. *Combustion Science and Technology, 123*(1–6), 287–315.
Li, S., Ren, Y., Biswas, P., & Stephen, D. T. (2016). Flame aerosol synthesis of nanostructured materials and functional devices: Processing, modeling, and diagnostics. *Progress in Energy and Combustion Science, 55*, 1–59.
Lu, J., Nordsiek, H., Saw, E. W., & Shaw, R. A. (2010). Clustering of charged inertial particles in turbulence. *Physical Review Letters, 104*(18), Article 184505.
Lu, J., & Shaw, R. A. (2015). Charged particle dynamics in turbulence: Theory and direct numerical simulations. *Physics of Fluids, 27*(6), Article 065111.
Maxey, M. R., & Riley, J. J. (1983). Equation of motion for a small rigid sphere in a nonuniform flow. *The Physics of Fluids, 26*(4), 883–889.
McQuarrie, D. A. (1976). *Statistical mechanics*. New York: Harper & Row.
Mofakham, A. A., & Ahmadi, G. (2019). Particles dispersion and deposition in inhomogeneous turbulent flows using continuous random walk models. *Physics of Fluids, 31*(8), Article 083301.
Morán, J., Poux, A., & Yon, J. (2021). Impact of the competition between aggregation and surface growth on the morphology of soot particles formed in an ethylene laminar premixed flame. *Journal of Aerosol Science, 152*, Article 105690.
Mortimer, L. F., Njobuenwu, D. O., & Fairweather, M. (2020). Agglomeration dynamics in liquid–solid particle-laden turbulent channel flows using an energy-based deterministic approach. *Physics of Fluids, 32*(4), Article 043301.
Njobuenwu, D. O., & Fairweather, M. (2018). Large eddy simulation of particle agglomeration with shear breakup in turbulent channel flow. *Physics of Fluids, 30*(6), Article 063303.
Polovnikov, P. V., Azarov, I. B., & Veshchunov, M. S. (2016). Advancement of the kinetic approach to Brownian coagulation on the base of the Langevin theory. *J. Aerosol. Sci., 96*, 14–23.
Pope, S. B. (2000). *Turbulent flows*. Cambridge university press.
Pumir, A., & Wilkinson, M. (2016). Collisional aggregation due to turbulence. *Annual Review of Condensed Matter Physics, 7*, 141–170.
Qian, W., Kronenburg, A., Hui, X., Lin, Y., & Karsch, M. (2022). Effects of agglomerate characteristics on their collision kernels in the free molecular regime. *Journal of Aerosol Science, 159*, Article 105868.
Rai, D. K., Beaucage, G., Vogtt, K., Ilavsky, J., & Kammler, H. K. (2018). In situ study of aggregate topology during growth of pyrolytic silica. *Journal of Aerosol Science, 118*, 34–44.
Ramkrishna, D., & Singh, M. R. (2014). Population balance modeling: Current status and future prospects. *Annual Review of Chemical and Biomolecular Engineering, 5*, 123–146.
Ray, B., & Collins, L. R. (2011). Preferential concentration and relative velocity statistics of inertial particles in Navier–Stokes turbulence with and without filtering. *Journal of Fluid Mechanics, 680*, 488–510.
Reade, W. C., & Collins, L. R. (2000). Effect of preferential concentration on turbulent collision rates. *Physics of Fluids, 12*(10), 2530–2540.
Renault, F., Sancey, B., Charles, J., Morin-Crini, N., Badot, P. M., Winterton, P., & Crini, G. (2009). Chitosan flocculation of cardboard-mill secondary biological wastewater. *Chemical Engineering Journal, 155*(3), 775–783.
Ruan, X., Chen, S., & Li, S. (2021). Effect of long-range Coulomb repulsion on adhesive particle agglomeration in homogeneous isotropic turbulence. *Journal of Fluid Mechanics*, 915.
Saffman, P. G. F., & Turner, J. S. (1956). On the collision of drops in turbulent clouds. *Journal of Fluid Mechanics, 1*(1), 16–30.
Saw, E. W., Shaw, R. A., Ayyalasomayajula, S., Chuang, P. Y., & Gylfason, A. (2008). Inertial clustering of particles in high-Reynolds-number turbulence. *Physical Review Letters, 100*(21), Article 214501.
Sharma, G., Dhawan, S., Reed, N., Chakrabarty, R., & Biswas, P. (2019). Collisional growth rate and correction factor for TiO2 nanoparticles at high temperatures in free molecular regime. *Journal of Aerosol Science, 127*, 27–37.
Squires, K. D., & Eaton, J. K. (1991). Preferential concentration of particles by turbulence. *Physics of Fluids A: Fluid Dynamics, 3*(5), 1169–1178.
Suh, S. M., Zachariah, M. R., & Girshick, S. L. (2001). Modeling particle formation during low-pressure silane oxidation: Detailed chemical kinetics and aerosol dynamics. *Journal of Vacuum Science and Technology A: Vacuum, Surfaces, and Films, 19*(3), 940–951.
Sundaram, S., & Collins, L. R. (1997). Collision statistics in an isotropic particle-laden turbulent suspension. Part 1. Direct numerical simulations. *Journal of Fluid Mechanics, 335*, 75–109.
Suresh, V., & Gopalakrishnan, R. (2021). Tutorial: Langevin dynamics methods for aerosol particle trajectory simulations and collision rate constant modeling. *Journal of Aerosol Science, 155*, Article 105746.
Tagawa, Y., Mercado, J. M., Prakash, V. N., Calzavarini, E., Sun, C., & Lohse, D. (2012). Three-dimensional Lagrangian Voronoï analysis for clustering of particles and bubbles in turbulence. *Journal of Fluid Mechanics, 693*, 201–215.
Tsouris, C., & Scott, T. C. (1995). Flocculation of paramagnetic particles in a magnetic field. *Journal of Colloid and Interface Science, 171*(2), 319–330.
Verma, A. K., Dash, R. R., & Bhunia, P. (2012). A review on chemical coagulation/flocculation technologies for removal of colour from textile wastewaters. *Journal of Environmental Management, 93*(1), 154–168.
Voßkuhle, M., Lévêque, E., Wilkinson, M., & Pumir, A. (2013). Multiple collisions in turbulent flows. *Phys. Rev. E, 88*(6), Article 063008.
Wang, Y., & Chung, S. H. (2019). Soot formation in laminar counterflow flames. *Progress in Energy and Combustion Science, 74*, 152–238.
Wang, K., Peng, W., & Yu, S. (2019). A new approximation approach for analytically solving the population balance equation due to thermophoretic coagulation. *Journal of Aerosol Science, 128*, 125–137.

Wang, L. P., Wexler, A. S., & Zhou, Y. (2000). Statistical mechanical description and modelling of turbulent collision of inertial particles. *Journal of Fluid Mechanics, 415*, 117–153.
Wilkinson, M., Mehlig, B., & Bezuglyy, V. (2006). Caustic activation of rain showers. *Physical Review Letters, 97*(4), Article 048501.
Yuan, W., Zhao, L., Andersson, H. I., & Deng, J. (2018). Three-dimensional Voronoï analysis of preferential concentration of spheroidal particles in wall turbulence. *Physics of Fluids, 30*(6), Article 063304.
Zhang, Y., Li, S., Yan, W., Yao, Q., & Tse, S. D. (2011). Role of dipole–dipole interaction on enhancing Brownian coagulation of charge-neutral nanoparticles in the free molecular regime. *Journal of Chemical Physics, 134*(8), Article 084501.
Zhang, H., Sharma, G., Dhawan, S., Dhanraj, D., Li, Z., & Biswas, P. (2020). Comparison of discrete, discrete-sectional, modal and moment models for aerosol dynamics simulations. *Aerosol Science and Technology, 54*(7), 739–760.
Zhang, Y., Xiong, G., Li, S., Dong, Z., Buckley, S. G., & Stephen, D. T. (2013). Novel low-intensity phase-selective laser-induced breakdown spectroscopy of TiO2 nanoparticle aerosols during flame synthesis. *Combustion and Flame, 160*(3), 725–733.
Zhao, K., Vowinckel, B., Hsu, T. J., Köllner, T., Bai, B., & Meiburg, E. (2020). An efficient cellular flow model for cohesive particle flocculation in turbulence. *Journal of Fluid Mechanics*, 889.
Ziemann, P. J., & Atkinson, R. (2012). Kinetics, products, and mechanisms of secondary organic aerosol formation. *Chemical Society Reviews, 41*(19), 6582–6605.